ELSEVIER

Journal of Electron Spectroscopy and Related Phenomena 124 (2002) 263–279

JOURNAL OF ELECTRON SPECTROSCOPY and Related Phenomena

www.elsevier.com/locate/elspec

Spin-polarized Fermi surface mapping

M. Hoesch[a,b,*], T. Greber[a], V.N. Petrov[c], M. Muntwiler[a,b], M. Hengsberger[a], W. Auwärter[a], J. Osterwalder[a]

[a]*Physik-Institut, Winterthurerstr. 190, Universität Zürich-Irchel, 8057 Zürich, Switzerland*
[b]*SLS Project, Paul Scherrer Institut, 5232 Villigen PSI, Switzerland*
[c]*St. Petersburg Technical University, 29 Polytechnicheskaya Street, 195251 St Petersburg, Russia*

Received 9 December 2001; received in revised form 22 December 2001; accepted 21 January 2002

Abstract

The magnetic and electronic properties of itinerant ferromagnets and their interplay have been studied in the last few years by spin resolved electron spectroscopy on one hand and by high-resolution angle-resolved photoemission experiments on the other. We discuss how the two approaches can be combined in a high resolution electron spectrometer with spin resolution for angle-scanned Fermi surface mapping experiments. We have built this new instrument, which allows an advance into a deeper understanding of magnetic thin film or multilayer systems, where band structures become intricately dense in momentum space and where the magnetization direction can change from layer to layer. Spin-resolution is thus required to arrive at a correct assignment of spectral features. A fully three-dimensional polarimeter makes the instrument 'complete' in the sense that all properties of the photoelectron are measured. First experiments on Ni(111) conclusively confirm previous band and spin assignments at the Fermi level and demonstrate the correct functioning of the apparatus.

Keywords: Photoemission; Itinerant ferromagnetism; Magnetic multilayers; Spin polarization; Fermi surface; Nickel; Surface electronic structure; Interface effects

1. Introduction

Recent advances in physics, chemistry and materials science have made it possible to produce artificial magnetic materials, i.e. materials that are far away from thermal equilibrium and do not exist in nature. They are often structured on the nanometer scale, and there is increasing evidence that electronic and magnetic properties can be tailored by controlling the structuring [1]. New ideas for devices based on such structures have opened the promising field of *magnetoelectronics* or *spintronics* [2]. While the preparation of laterally structured devices is still in its infancy, the production of layered artificial structures, that can be prepared by sophisticated growth methods, has matured in recent years. Multilayers of alternating magnetic and non-magnetic metals are now finding their way into the markets as sensors in magnetic recording heads.

In order to obtain a fundamental understanding of such systems and how their properties can be engineered, we need to have a detailed picture of their electronic structure and how it varies when the artificial structuring is changed. Of particular impor-

*Corresponding author. Tel.: +41-1-635-5824; fax: +41-1-635-5704.
E-mail address: mhoesch@physik.unizh.ch (M. Hoesch).

0368-2048/02/$ – see front matter
PII: S0368-2048(02)00058-0

tance are the electrons near the Fermi energy and their momentum distribution, i.e. the Fermi surface. In magnetic multilayers, e.g. a clear correlation has been found between Fermi level crossings of quantum well states, which can be tuned by varying the interlayer thickness, and the oscillatory coupling (ferromagnetic vs. antiferromagnetic) between the magnetic layers [3]. The classical Fermi surface probes, such as the de-Haas-van-Alphen effect, positron annihilation or Compton scattering, cannot be used for these kinds of samples because they are essentially bulk probes. On the other hand, Fourier analysis of scanning-tunneling microscopy/spectroscopy images, which was recently introduced as a new Fermi surface probe [4], has been demonstrated only for surface states on noble metal and simple metal surfaces, and it lacks momentum resolution perpendicular to the layer plane. Angle-resolved photoemission (ARUPS) thus remains as the prime technique to study the electronic structure and the Fermi surface of such nanostructured magnetic samples, where quantized bulk states are believed to play a crucial role for the magnetic coupling between magnetic layers.

The traditional procedure in ARUPS experiments was to locate Fermi level crossings of energy bands in angle-resolved photoemission spectra in order to trace Fermi surface contours [5]. Recently, a few groups have begun to map Fermi surfaces directly by measuring intensities of photoelectrons emitted from the Fermi edge as a function of emission angles relative to the crystal axes, and thus of the momentum component $\vec{k}_{\parallel}$ parallel to the surface [6,7]. At positions where a band crosses the Fermi level, the photoemission intensity at the Fermi edge rises sharply, contributing to the measured contour of the Fermi surface map. It has been demonstrated that this procedure produces accurate bulk and surface Fermi surface maps of noble metals, magnetic transition metals and even high-temperature superconductors [8]. A demonstration of the potential of photoemission mapping as applied to a magnetic system has recently been given. The Fermi surfaces of both minority and majority electrons in ferromagnetic Ni metal have been measured, as well as their behavior with temperature as the Curie temperature is approached and exceeded. In this case, the spin character of the bands was not measured directly but was inferred from comparing the measured Fermi surface contours to those obtained from a band structure calculation. The excellent agreement between the two made the assignment unambiguous [9,10].

It should be pointed out that for the case of a bulk ferromagnet like Ni metal one does not need to magnetize the sample in order to see the spin-split Fermi surfaces, because the local magnetization in each magnetic domain induces the same exchange splitting throughout the crystal, except for minor regions inside domain walls. Minority and majority spin character has thus a local meaning even though the sample as a whole is unmagnetized. However, in nanostructured materials such as e.g. magnetic multilayers, it is crucial to identify the relative spin character of electronic bands in the various magnetic layers as well as the spin polarization of sp-bands of the non-magnetic layers. For this purpose, a spin-resolved photoemission or inverse photoemission experiment must be carried out. Unfortunately, the measurement of the photoelectron spin polarization is very cumbersome, with typical devices (Mott detectors) having an overall efficiency of 10^{-3} to 10^{-4} compared to common spin-averaging detectors [11]. In order to make up for the reduced sensitivity, spin-resolved experiments usually have to make strong compromises in energy and angular resolution, and one thus sacrifices the wealth of information near the Fermi level available with high-resolution photoemission [12].

In magnetic nanostructures, such as e.g. multilayers, the presence of new boundary conditions or new periodicities of the order of one nanometer makes those dimensions in reciprocal space become smaller by typically one order of magnitude. This is illustrated in Fig. 1. An idealized $Co_5Cu_4(111)$ magnetic multilayer is depicted in (a), which has a superperiodicity of nine atomic layers in the vertical direction. Fig. 1b shows the Fermi surface contours of bulk Cu and of face-centered-cubic (fcc) bulk Co (majority spin) within the $(1\bar{1}\bar{2})$ plane of the fcc reciprocal lattice. Slab calculations for the multilayer [13] produce the closely spaced Fermi surface sheets that are plotted inside the vertically compressed hexagonal Brillouin zone. The extended zone scheme for the multilayer will thus show a very dense manifold of Fermi surface sheets. As is outlined in Section 2, this leads to closely spaced Fermi surface

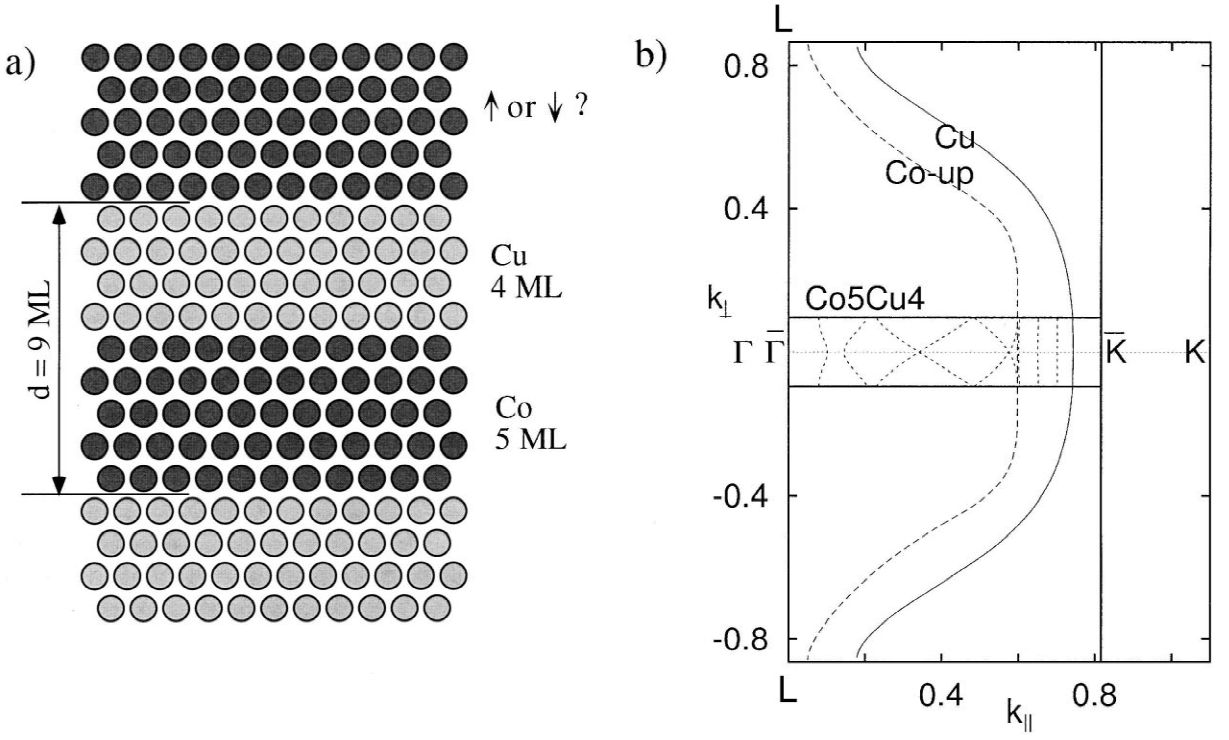

Fig. 1. (a) Schematic section through a magnetic multilayer consisting of an alternative stacking of five monolayers (ML) of fcc Co and 4 ML of Cu. (b) Cuts through Fermi surfaces of bulk copper, majority bulk cobalt, and through the majority Fermi surface of the periodic $Co_5Cu_4(111)$ multilayer of (a). The labels $\bar{\Gamma}$ and $\bar{K}$ refer to points at the center and corners, respectively, of the hexagonal two-dimensional Brillouin zone of the multilayer, while Γ, K and L refer to high-symmetry points in the three-dimensional Brillouin zone of the fcc lattice. $k_{\parallel}$ and $k_{\perp}$ are expressed in units of $2\pi/a$, where a is the fcc lattice constant (from Ref. [13]).

contours in photoemission Fermi surface maps. This example shows that high momentum resolution is a prerequisite in order to obtain relevant Fermi surface data for such systems and that it must not be compromised when spin detection is employed.

We have thus designed and built a new spin- and angle-resolved photoemission spectrometer that should meet the specifications required for measuring spin-resolved Fermi surfaces at sufficiently high energy and angular resolution. In doing so we had to overcome two major obstacles: (i) the sensitivity problem and (ii) the magnetization direction problem. The sensitivity problem due to the low detection efficiency of current spin polarimeters is solved using high flux synchrotron light from a third-generation source for excitation, and by combining spin-resolved and spin-averaged photoelectron spectroscopy simultaneously in the same electron analyzer. One can thus conveniently take a spin-averaged global map of Fermi surface contours before homing in on selected contours for polarization analysis. The second obstacle is more fundamental: a spin polarimeter based on Mott scattering can measure the spin polarization of photoelectrons along two axes that are fixed in space (see Section 3). Unfortunately this is not sufficient. The measurement of Fermi surface maps requires free rotation of the sample, and of its magnetization direction, about two independent axes. In order to trace the polarization vector of the electrons throughout the complete map, one has thus to measure all three spin components. We have chosen a design based on two complete Mott polarimeters, thus measuring altogether four spin projections (see Section 4). The one redundant projection is selected to provide a useful cross check for the spin polarization along one fixed axis. Since

all quantum numbers of a photoelectron—momentum and spin—are measured in this spectrometer, it can be regarded as complete, hence the name COmplete PHotoEmission Experiment (COPHEE). A similar design has been described by Chen [14].

The interest in spin-resolved Fermi surface mapping is not limited to magnetic nanostructures. There are several other pressing fundamental problems in solid state physics and surface science where this new spectrometer can bring significant advances. For instance, the spin-polarization of majority and minority Fermi surface contours on nickel can be measured as the Curie temperature is approached from below, and the interplay between magnetic fluctuations and the magnetic exchange splitting can be studied in detail [10]. Manybody-effects lead to strong momentum and spin-dependent band shifts and band broadening in measured photoemission spectra from the late 3d transition metals, even near the Fermi energy, compared to single-particle band structure calculations [15,16]. In cases where detailed manybody calculations are not available, such as, e.g. in alloys, the measurement of the electron spin is therefore very important for a correct assignment of the observed bands.

2. Fermi surface mapping by photoemission

Fermi surface mapping requires the measurement of the electron momentum, or wave vector $\vec{k}$, which is complicated by the fact that photoemission from crystalline surfaces conserves only the wave vector component $\vec{k}_{\parallel}$ parallel to the surface. The short probing depth and the propagation through the surface potential step broadens and reduces, respectively, the wave vector component $k_{\perp}$ perpendicular to the surface. Photoemission calculations within the one-step model [17] considering appropriate time-reversed low-energy electron diffraction (LEED) states as photoelectron final states can overcome this problem quantitatively. On the other hand, the much simpler three-step model [18] has proved quite successful when free-electron final states are used for describing the electron propagation through the solid to the surface (step 2) after the photoexcitation process (step 1) [19]. Transmission through the surface potential step (step 3), which is characterized by the inner potential V_0, can then be treated like a refraction at the boundary of two media: the free-electron plane wave outside the surface has a shorter $k_{\perp}$ than the one inside the solid.

From the measured photoelectron kinetic energy in vacuum

$$E^m_{\mathrm{kin}} = h\nu - \Phi - E_{\mathrm{B}} \tag{1}$$

where $h\nu$, Φ and E_{B} are photon energy, work function and binding energy measured from the Fermi level, respectively, and from the emission polar angle ϑ_m (measured from the surface normal), one calculates readily

$$|\vec{k}_{\parallel}| = \frac{1}{\hbar}\sqrt{2mE^m_{\mathrm{kin}}}\,\sin\vartheta_m \tag{2}$$

and

$$k_{\perp} = \frac{1}{\hbar}\sqrt{2m(E^m_{\mathrm{kin}} + V_0)}\,\cos\vartheta \tag{3}$$

where

$$\sin\vartheta = \sin\vartheta_m\sqrt{\frac{E^m_{\mathrm{kin}}}{E^m_{\mathrm{kin}} + V_0}} \tag{4}$$

is the sine of the refracted polar angle. Within the free-electron final-state approximation, these components define the $\vec{k}$-vector of the photo-hole inside the solid for a particular sample azimuth φ. Matters become simpler in two-dimensional systems such as surface states or ultrathin films, where only $\vec{k}_{\parallel}$ is relevant [20].

Constant energy maps or, more specifically, Fermi surface maps result from taking photoemission intensities at just one binding energy and scanning both emission angles over most of the hemisphere above the surface [7]. According to Eqs. (2) and (3), and including the rotation about the azimuthal angle φ, the sampled $\vec{k}$-vectors then sweep the surface of a spherical sector with a radius as described by

$$k = \frac{1}{\hbar}\sqrt{2m(E^m_{\mathrm{kin}} + V_0)} \tag{5}$$

and with its opening angle reduced by refraction

effects compared to the polar angle range measured outside the crystal.

This is illustrated in Fig. 2, which shows the $(\bar{1}\bar{1}0)$ plane in the reciprocal space of fcc Ni. The free-electron final states for excitation with He I (21.21 eV) and He II (40.8 eV) appear as circles centered at Γ_{000} in this plot, and the photoemission horizon, above which electrons can overcome the surface potential barrier, is indicated by the horizontal hatched line. Photoelectrons outside the surface will be measured at higher polar angles due to the refraction described in Eq. (4). In the extended zone scheme of Fig. 2, momentum conservation in the photoemission process means that transitions for a given photon energy occur wherever the two constant energy surfaces (initial and final state) with the proper energy separation intersect, as is shown for the case of the Fermi surface of nickel. It is required that the photoelectron picks up momentum from the lattice in the form of a reciprocal lattice vector. In the actual measurement, these intersections form continuous contours on a grey scale plot (see e.g. Fig. 3a), because the constant energy surfaces are continuous in three-dimensional momentum space.

The resulting Fermi surface contours can also be produced by applying the same intersection procedure to a band structure calculation. Fig. 3b demonstrates how well the experimental contours can be matched in the case of Ni, in this case for a measurement through the (111) surface. The agree-

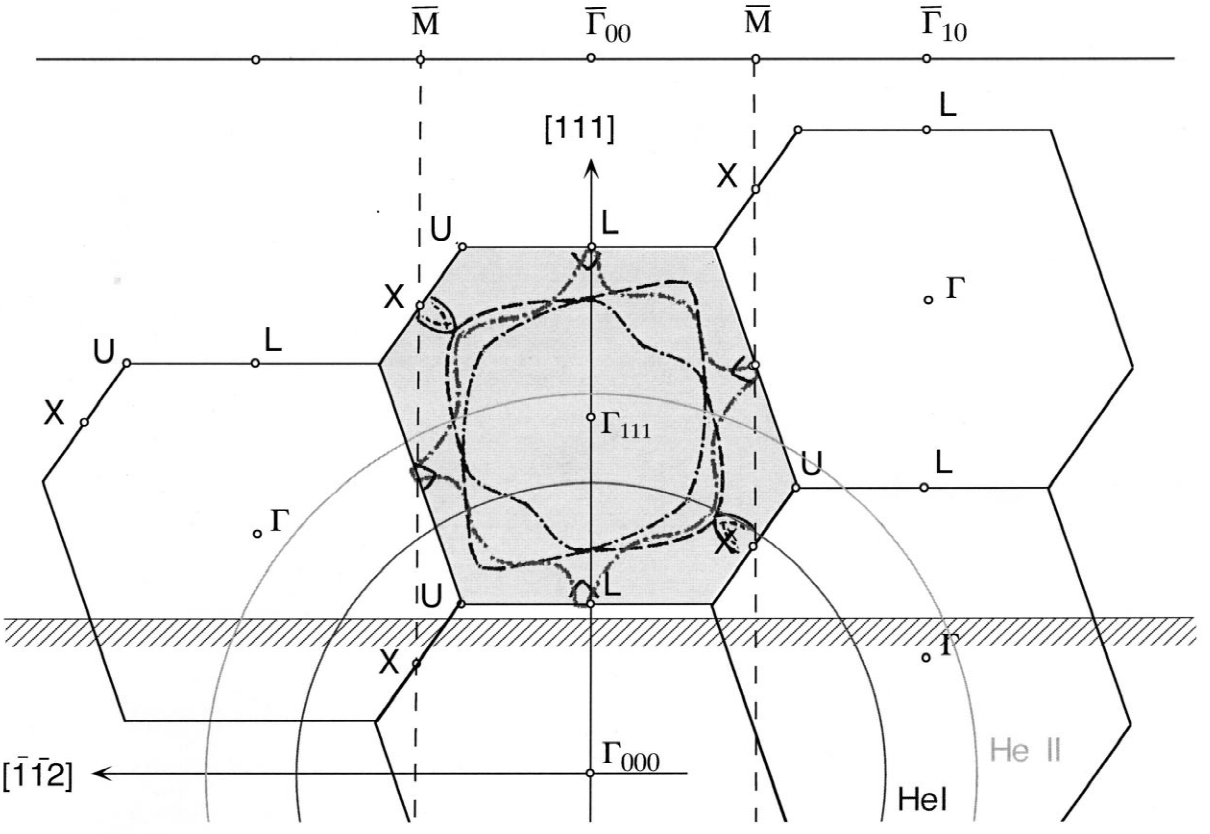

Fig. 2. Schematic diagram for *k*-space mapping experiments. In the free electron final state approximation direct transitions are expected if the final state sphere intersects with an initial state band in the extended zone scheme. $k_{\parallel}$ of these intersection points is conserved throughout the whole photoemission process. The photoemission horizon (hatched line) is imposed by the inner potential, which has to be overcome by the photoelectron travelling into vacuum.

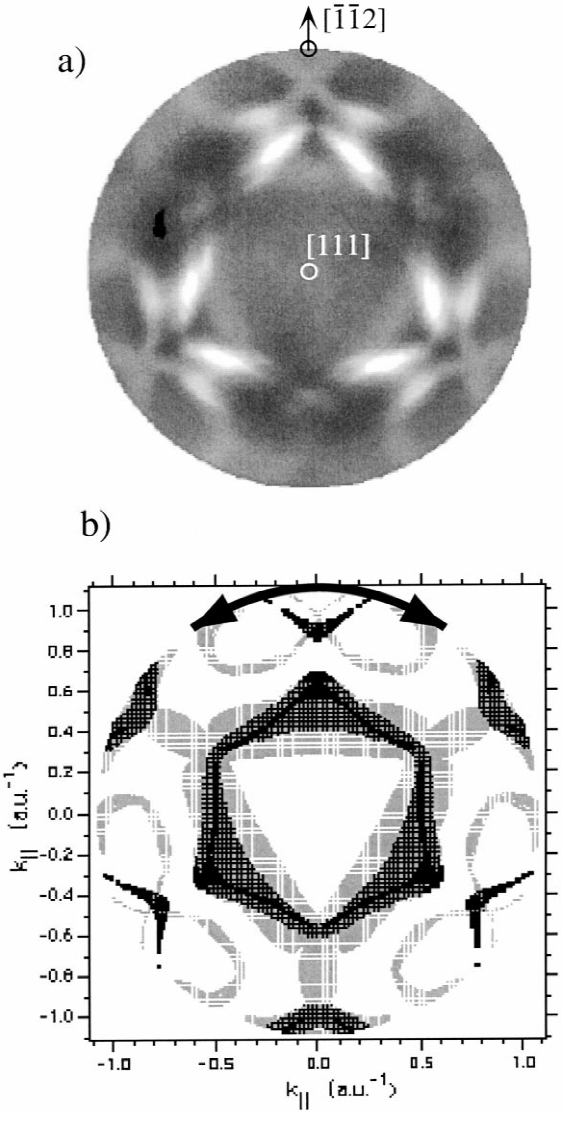

Fig. 3. (a) He Iα excited Fermi surface map ($h\nu = 21.21$ eV) from Ni(111). A $\vec{k}_{\parallel}$ projection of the raw data is presented in a linear grey scale, with highest intensities in white, lowest in black. In (b) the corresponding spin-polarized band structure calculation is displayed, showing Fermi level crossings at the same $\vec{k}_{\parallel}$ locations as in the measurement (a). Majority spin bands are shown in black, minority spin bands in grey. The region highlighted by a black arrow is discussed in Section 5 (figure from Ref. [21]).

ment is good enough to permit the assignment of the majority/minority character of the individual contours.

3. Spin polarimetry in three dimensions

To measure the spin polarization of electrons, a large variety of polarimeters have been devised since the discovery of the electron's magnetic moment. The classical method goes back to Mott's analysis of the elastic scattering of relativistic electrons with atomic nuclei [22], which predicted an asymmetry in the backscattered intensities N_L, N_R measured on the left and right of the incoming beam in a common scattering plane. The polarization component P_x in the direction perpendicular to the scattering plane is determined from the asymmetry

$$A_x = \frac{(N_L - N_R)}{(N_L + N_R)} \tag{6}$$

and the so-called Sherman function S [23] as

$$P_x = A_x / S \tag{7}$$

The Sherman function is the asymmetry that would be measured in the case of a 100% polarized beam. It determines the analyzing power of the process and of the detection geometry. The overall efficiency of a polarimeter can be judged from the figure of merit

$$\varepsilon = (I/I_0)S^2 \tag{8}$$

where I/I_0 is the ratio of detected electrons to the total number of incoming electrons [24]. The statistical error due to the electron counting can be found as

$$\Delta A_x = 1/\sqrt{N_L + N_R} \tag{9}$$

For a given number N_0 of incoming electrons, the statistical error of P_x is thus given by $\Delta P_x = 1/\sqrt{\varepsilon N_0}$. In this sense, the figure of merit corresponds to the detection efficiency for spin polarization. Typical figures range between $\varepsilon = 10^{-4}$ and $\varepsilon = 10^{-3}$.

The scattering plane is spanned by the incoming beam and the positions of the detectors for left and right scattering. In a single polarimeter it is therefore possible to measure the two transverse polarization components of an electron beam by arranging four detectors in two orthogonal scattering planes in front of the target.

In a real Mott polarimeter, the electrons have to be accelerated to relativistic energies and then detected

in an energy sensitive way to filter the signal from inelastically scattered electrons, which would otherwise wash out the polarization sensitivity. The basic physical process which is responsible for the difference between backscattering to the left and the right is the spin–orbit interaction in the potential of the atomic nucleus. The effect is stronger the heavier the target nuclei, and gold foils represent an optimum compromise between high atomic number and target inertness.

For our experiment we chose a polarimeter [25] in which the electrostatic acceleration voltage is 60 kV and the detectors are energy sensitive silicon diodes operated in reverse bias with a variable discriminator threshold. The detectors with the amplifiers and discriminators are floated on top of the acceleration voltage to allow a field-free travel of the electrons from the scattering gold foil to the detectors. The acceleration field is provided by two concentric hemispheres thereby giving a highly focusing spherical field. These two electron optical features reduce the polarimeter's sensitivity to slight motions or changes in shape of the incoming beam [26]. The design of these polarimeters goes back to the classical Mott polarimeters operating at 100 to 120 keV [27], yet they can be combined with a conventional energy analyzer due to their compactness.

A second class of Mott polarimeters re-decelerates the electrons to near ground potential after the scattering, using a retarding field which can only be overcome by the elastically scattered electrons. These detectors, named mini-Mott polarimeters, can work at much lower accelerating voltages of typically 25 kV and can be more easily combined with spectroscopic equipment. The development of these devices [28,29] is very advanced and detailed numerical analyses have been employed for their optimization [30,31]. The electron optical acceptance is very high, but the fact that the filtering of inelastically scattered electrons is also based on electron optics makes them sensitive to the condition of the incoming beam, which can give rise to spurious effects in a scanned experiment [26].

In addition to these polarimeters operating at relativistic energies, which can truly be called Mott detectors, there is also a class of polarimeters based on scattering at lower kinetic energies. Very high efficiencies have been achieved by Low Energy Electron Diffraction (LEED) scattering, where the left–right detectors collect the signal from two equivalent diffraction spots from a tungsten single crystal surface [32]. Also in diffuse scattering from Au surfaces at low energies a good figure of merit has been demonstrated because of the high total reflectivity for slow electrons [33], and these polarimeters, also measuring a left–right asymmetry of reflected electrons, have been successfully employed for electron spectroscopy applications. Due to the high surface sensitivity at low energies, these polarimeters require frequent conditioning of the scattering target, and the performance is subject to continuous change even in good vacuum.

In addition to polarimeters based on backscattering, a number of other effects in the interaction of polarized electrons with solids have been employed for polarimetry. An absorption detector measures the spin-dependent absorption on a metal surface [11]. A promising recent development are transmission detectors based on the spin filter effect of a ferromagnetic film. The high analyzing power of the spin filtering based on the exchange interaction can lead to a very high figure of merit. For practical applications, the total transmission still needs to be improved. It is limited by the large amount of support material needed to make the films free standing.

All polarimeters based on scattering have the common limitation that they can only detect the two polarization components transverse to the incoming beam. In an electrostatic beam deflection system the spin remains fixed in space from the sample to the detector. If a certain polarization component in the sample is to be analyzed, the orientation of the detector has to be chosen accordingly. The complete three-dimensional polarization vector can be analyzed by sending the electrons to two independent, orthogonally mounted polarimeters. This concept is shown schematically in Fig. 4. In this design, the polarization component P_z along the entrance lens axis of the analyzer, i.e. the longitudinal polarization of the photoelectrons, is covered by both polarimeters, a redundancy which can be used to enhance the sensitivity in this component and to cross-check in the course of data taking. If we label the eight detectors according to Fig. 4 we find the full polarization vector $\vec{P}$ as

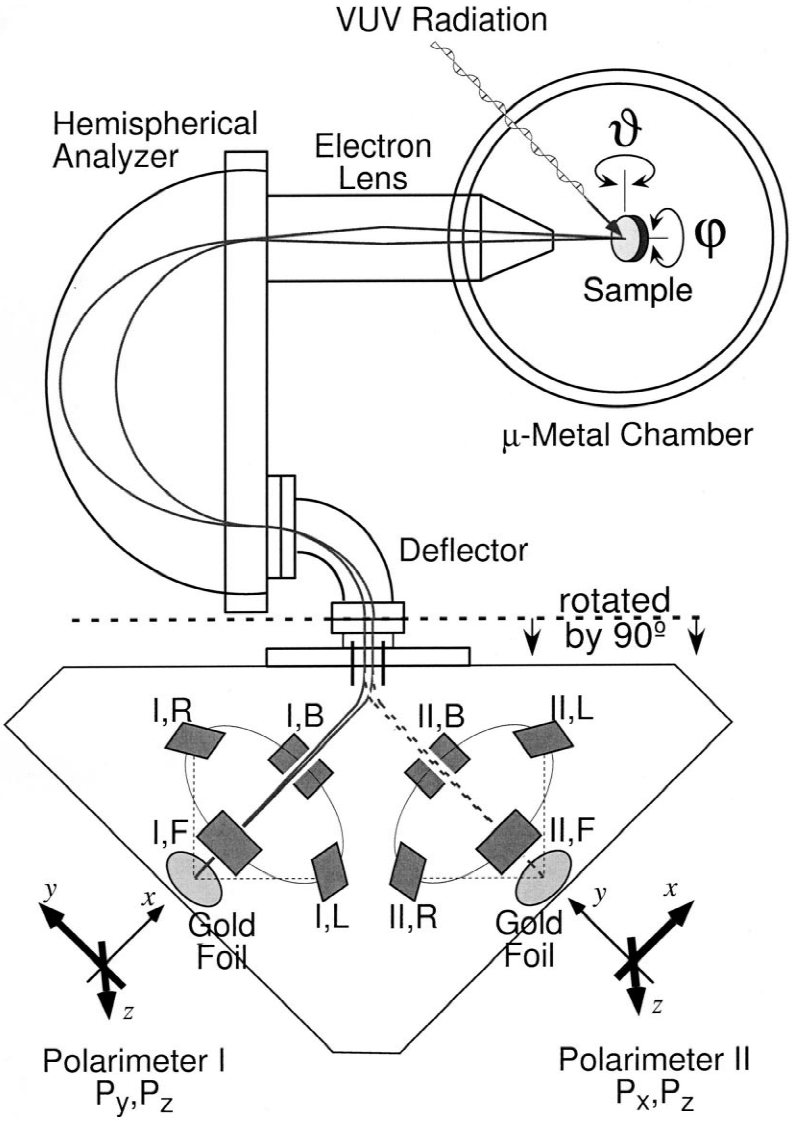

Fig. 4. Schematic view of COPHEE, the COmplete PHotoEmission Experiment. Electrons photoemitted from a sample by UV radiation are energy- and angle-selected by an electrostatic analyzer and detected in two orthogonal Mott polarimeters. In an electrostatic beam deflection system the spin direction is conserved and polarimeter I measures the polarization components P_y and P_z, while polarimeter II measures P_x and P_z. The beam is switched between the two to allow quasi-simultaneous data collection. The labels of the detectors are used in Eq. (10) in the text. The polarimeter system is shown rotated by 90° for graphical clarity.

$$P_x = \frac{1}{S}\frac{(N_{\mathrm{II,B}} - N_{\mathrm{II,F}})}{(N_{\mathrm{II,B}} + N_{\mathrm{II,F}})}, \quad P_y = \frac{1}{S}\frac{(N_{\mathrm{I,F}} - N_{\mathrm{I,B}})}{(N_{\mathrm{I,F}} + N_{\mathrm{I,B}})},$$
$$P_z = \frac{1}{2}\frac{1}{S}\left(\frac{(N_{\mathrm{I,L}} - N_{\mathrm{I,R}})}{(N_{\mathrm{I,L}} + N_{\mathrm{I,R}})} + \frac{(N_{\mathrm{II,L}} - N_{\mathrm{II,R}})}{(N_{\mathrm{II,L}} + N_{\mathrm{II,R}})}\right) \quad (10)$$

If we consider the rotations of the sample manipulator (given by the angles ϑ and φ), we can represent the polarization vector $P^{(\mathrm{S})}$ in the sample coordinate system given by the sample normal $\hat{z}_{\mathrm{S}}$ and some axis $\hat{x}_{\mathrm{S}}$ in the surface plane through a

rotation matrix which can be found by Euler rotations:

$$\begin{pmatrix} P_x^{(S)} \\ P_y^{(S)} \\ P_z^{(S)} \end{pmatrix} = \begin{pmatrix} \frac{\cos\vartheta\cos\varphi - \sin\varphi}{\sqrt{2}} & \frac{-\cos\vartheta\cos\varphi - \sin\varphi}{\sqrt{2}} & \sin\vartheta\cos\varphi \\ \frac{\cos\vartheta\sin\varphi + \cos\varphi}{\sqrt{2}} & \frac{-\cos\vartheta\sin\varphi + \cos\varphi}{\sqrt{2}} & \sin\vartheta\sin\varphi \\ \frac{-\sin\vartheta}{\sqrt{2}} & \frac{\sin\vartheta}{\sqrt{2}} & \cos\vartheta \end{pmatrix} \times \begin{pmatrix} P_x \\ P_y \\ P_z \end{pmatrix} \quad (11)$$

The polarization vector, which is the vector of expectation values of the three spin component operators S_x, S_y and S_z, is an observable and therefore transforms like a classical vector. It should be noted that the measurements to determine the expectation values are carried out on separate sets of electrons [24].

4. Experimental design

The COPHEE set-up is shown in Fig. 5. It is designed to be flexible for use as a synchrotron radiation end station or as a stand-alone experiment. The system can be attached as a second end-station to the Surface and Interface Spectroscopy (SIS) beamline at the Swiss Light Source (SLS) in Villigen, Switzerland [34]. The spectrometer part, consisting of the electron energy analyzer and the polarimeters, is also compatible with the end station of the Advanced Photoemission Low Energy (APE-LE) beam line at the ELETTRA synchrotron light source in Trieste, Italy [35]. A high flux helium lamp is mounted, that permits operation independently of the synchrotron (type VUV 5000 from Gammadata Burklint AB, Sweden [36]).

The system consists of a μ-metal analysis chamber, which houses the light sources (twin anode Si and Mg X-ray source and helium lamp) and the analyzer entrance lens, and which connects to the synchrotron beamline. Above, a stainless steel preparation chamber provides Ar^+-sputtering and evaporation sources, a gas inlet as well as low-energy electron diffraction (LEED) equipment and spare ports for additional sample preparation and characterization tools. Sample transfer to the extended facilities of the SIS beamline station is possible when the chamber is placed on the beam line. A sample manipulator is introduced from above through the preparation chamber. A base pressure of 10^{-10} mbar is achieved by pumping using turbomolecular, ion getter and rare earth evaporator pumps.

The manipulator consists of a motion stage, which allows positioning of the sample and transfer between the preparation and the analysis chambers (400 mm travel). Sample rotations by a home built two-axis goniometer [37] give the choice of any emission angle for photoelectron spectroscopy (Fig. 6). Sample cooling (liquid He or N_2) and heating, as well as magnetization switching, can be carried out at any angular setting and during scans. The sample is attached to the goniometer on the standardized 'Swiss Stub' sample holder, which provides sliding contacts for heating and magnetizing currents and which can be removed from the manipulator for sample transfer and in situ exchange of samples using a wobble stick. A special picture frame sample shape has been developed for achieving a sizeable remnant sample magnetization and low magnetic stray fields above the sample surface (Fig. 6b,c).

With the choice of soft X-rays and VUV light, experiments in the X-ray Photoelectron Diffraction (XPD) regime are possible in the same set-up as the ARUPS measurements. This allows for sample characterization as well as complementary studies in which both the atomic arrangement and the electronics structure are investigated. The SIS beamline [34] is designed to provide high photon flux in an energy range of $h\nu = 10$–800 eV at resolutions $\Delta E/E < 10^{-4}$. The light polarization from the electromagnetic crossed field undulator can be chosen linear or circular with both helicities. Of high importance for Fermi surface mapping experiments is the absence of higher energy photons in the light spectrum. This is achieved by employing a quasi-periodic magnetic structure in the undulator, which shifts the higher harmonics to non-integral multiples of the fundamental and allows subsequent filtering of the higher order photons in the monochromator. For the lowest photon energies a normal incidence monochromator is used instead of the plane grating

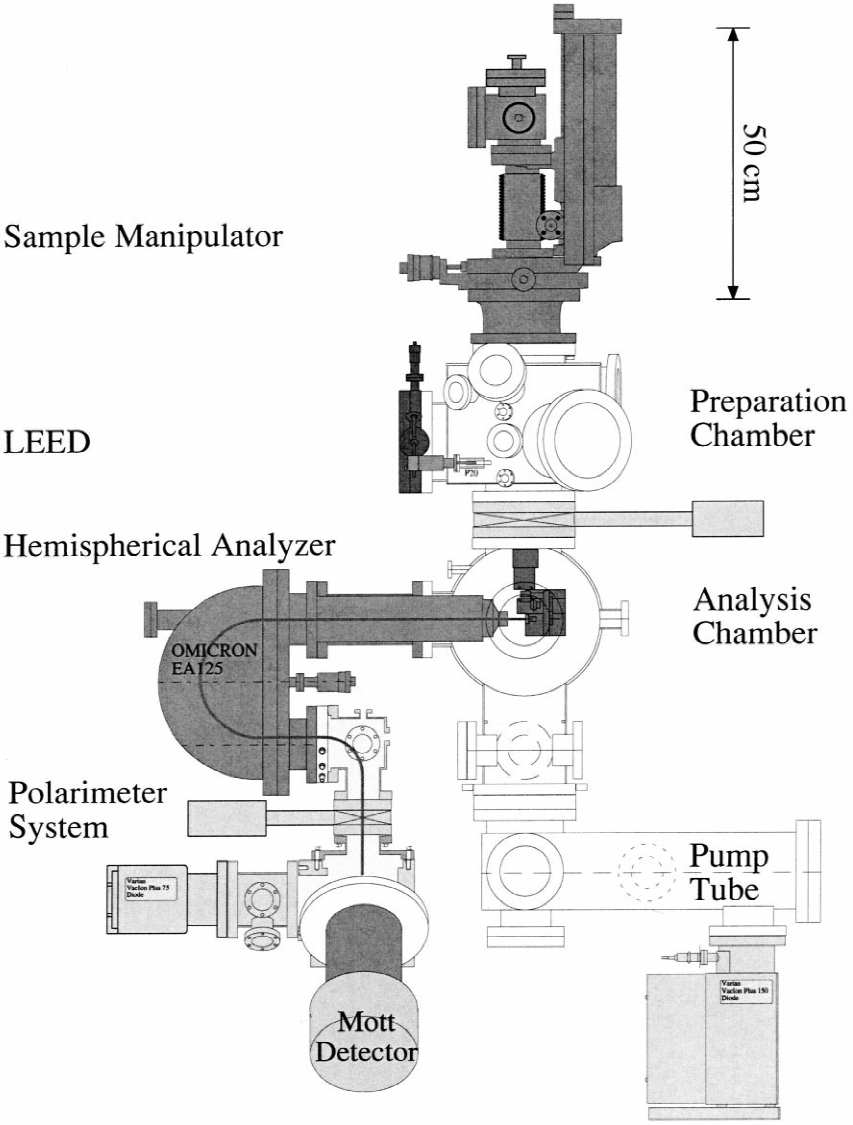

Fig. 5. Drawing of the COPHEE set-up consisting of the analysis and preparation chambers with the sample manipulator and the analyzer and polarimeters as well as a pump tube.

monochromator, providing additional filtering of parasitic higher energy light.

The electron spectrometer is an EA125 electrostatic hemispherical analyzer from Omicron Vacuumphysik GmbH, Germany. It consists of a two-stage lens with variable magnification and a 124-mm mean radius 180° deflector. The detector set-up was modified by Omicron from the original seven-channel version to a three channeltron detector for spin integrated measurements and an accelerating extraction lens for transport of the photoelectrons into the polarimeters.

The polarimeters have been briefly described in Section 3 and a detailed account is given in Ref. [25]. For the specific needs of photoelectron spectroscopy, the detector electronics have been redesigned. To achieve a high dynamic range of the detector, low noise operation with dark counts

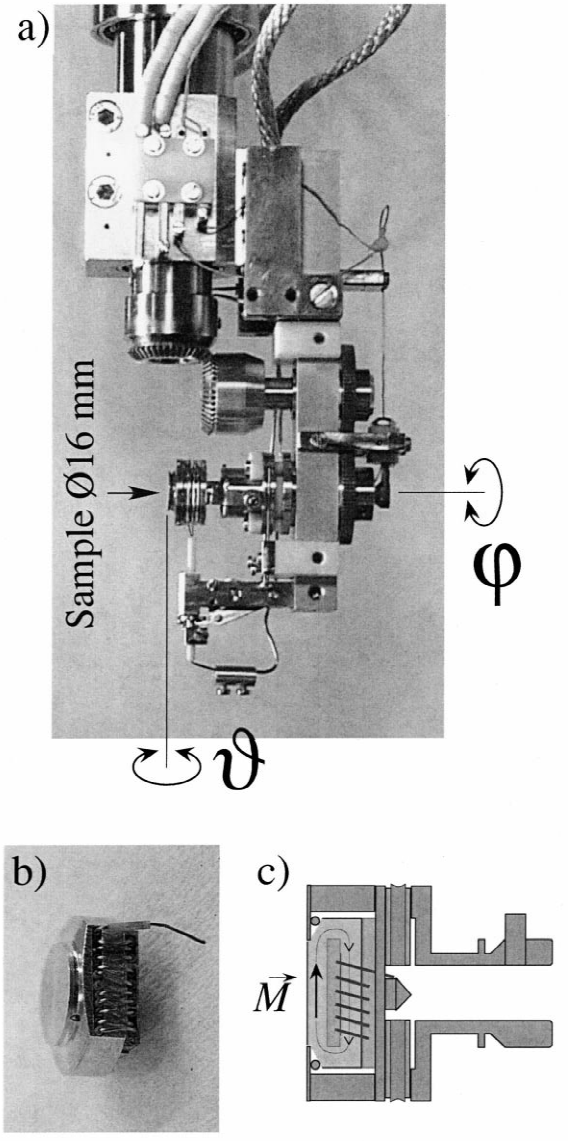

Fig. 6. (a) Goniometer head of the in-vacuum manipulator. The gears for the azimuthal rotation and the sliding contacts can be seen. Rotation about the manipulator axis provides the polar angle degree of freedom. Parts of the cooling system have been removed and only the cooling braids for the radiation shield are visible. (b) Photograph of a nickel picture frame sample with the filament for heating and magnetizing. The sample was cut from a Ni(111) disk by spark erosion [38]. (c) Drawing of the Swiss Stub sample holder, which allows in-situ exchange of samples on the manipulator. A picture frame sample is shown as mounted and the groove for the heating contact can be seen. The magnetization vector M is indicated. The frame is closed below the polished sample surface where the windings of the coil are shown.

limited only by cosmic background radiation must be possible. At the same time the maximum count rate is rather moderate due to the high resolution of the energy and angular filters and the low reflectivity of the gold foil. The pre-amplifier was completely redesigned with an increased shaping time and the original Silicon Surface Barrier (SSB) sensors were replaced by diodes manufactured by the Passivated Implanted Planar Silicon (PIPS) process.

The largest task in realizing COPHEE, which we describe in more detail here, was the design of a transport electron optical system including a two-way switch to inject the electrons coming from the analyzer into the Mott detectors. The requirements are: (i) a chromatic range of a decade if the optics are to be used in identical mode at analyzer pass energies from 1 to 10 eV; (ii) a high transmission close to 100% to prevent further loss of signal in this flux-hungry experiment; (iii) space constraints due to the different chambers to which the system must be compatible and the large size of the Mott detectors and the necessity of a vacuum valve to separate the Mott detectors, containing the sensitive gold foils, from the main chamber during sample preparation and maintenance.

(i) Any electron optical system behaves identical at different kinetic energies if all electrode voltages are scaled proportional to the energy. In our case, the relevant energy is the analyzer pass energy and the reference potential for the voltages is the Herzog plate of the analyzer. The extraction lens made by Omicron is designed to form a narrow beam with small angular spread if a total acceleration to 300 times the pass energy is used. This means that the kinetic energy in the beam transport system is $E'_{\mathrm{p}} =$ 300–3000 eV if a pass energy range of $E_{\mathrm{p}} = 1$–10 eV is covered. Consequently, the lens system has to withstand rather high voltages up to 5 kV and at the same time fine tuning of the voltages must be possible. In particular, the parallel plate deflector voltages (see below) must be switched at ± 1 kV fast enough to provide a long plateaux of stable electrostatic operation where data can be collected.

(ii) The finite size and angular spread of the photoelectron source at the sample position do not allow to form a parallel beam. Therefore several focusing elements have to be employed in the beam transport. The electron-optical layout is shown in

Fig. 7. The extraction lens forms a beam waist at its end. This point is imaged by the doubly focusing spherical field of the 90° deflector into the straight lens. In this position the lens tube is fourfold split along the beam axis and individual voltages on the elements allow slight corrections. The electrodes directly adjacent to the gap for the gate valve are held at reduced voltage and provide an Einzel lens together with the ground potential of the vacuum envelope. Furthermore the valve's inner diameter was chosen rather large (65 mm) and the Einzel lens electrodes are expanded to plates parallel to the valve to reduce the field of the ground potential and any unwanted (non-cylindrical) effects it might have. A third beam waist forms at the entrance into the switched deflector. The end deflector is made of the same spherical elements as the 90° deflector and also provides some focusing. Right before the highly focusing field of the 60 kV acceleration a final cylindrical acceleration lens allows fine tuning of the injection into the Mott detector. All fringe field terminations of the deflecting elements were chosen to give smooth transitions without accelerations between the drift and the deflection zones.

A solution to (iii) was found by first deflecting the electrons 90° in the plane of deflection of the analyzer and then through a straight lens which includes a gate valve. The valve necessarily introduces a gap in the high voltage lens cylinders, where the electrons 'see' the grounded vacuum tube. After the valve the beam is slightly deflected to the left or right by a symmetric parallel plate deflector, which can be switched and then further deflected to a total of 45° to give the 90° separation between the two

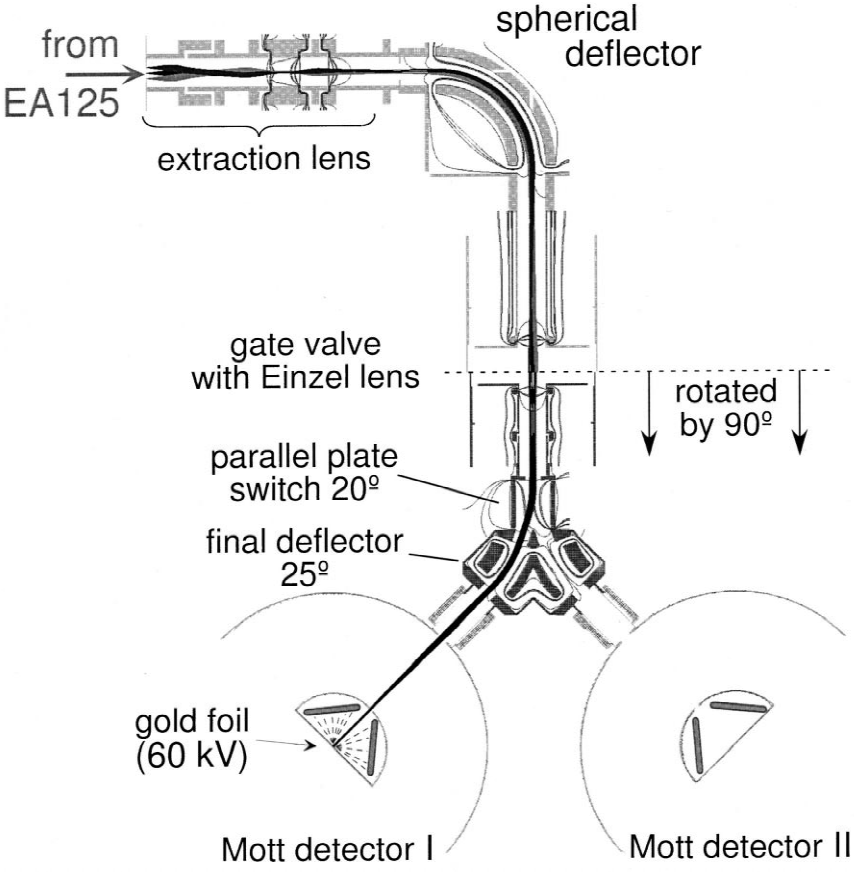

Fig. 7. Cut through the beam transport lens with the polarimeter assembly rotated by 90° for graphical clarity. The system is described in the text. Ray-tracing and graphics made using SIMION 6.0 [39].

beams required by the orthogonality of the polarimeters. In this design the Mott detectors are mounted below the analyzer, where enough space is available and the chance for clashes with future additions to the instrument (e.g. additional sample preparation facilities) is small.

The mechanical set-up of the beam transport system is based on two stainless steel vacuum chambers for the deflector and the switch. The switch chamber also houses the large outer hemispheres of the Mott detectors and the corresponding 250-mm o.d. flange seals. It was cut from a solid steel block at the workshop of the Physics Institute at Zurich University (Fig. 8b). The graphitized aluminum lens electrodes are insulated from each other by macor and alumina ceramics and held by aluminum supports in the flange faces of the two chamber entrance flanges. Electrical contacts to Safety High Voltage (SHV-5 kV) feedthroughs are made by Kapton coated copper wires. The electrode system before graphitizing and final assembly is shown in Fig. 8a.

5. Spectrometer performance

To demonstrate the performance of the COPHEE instrument, we discuss three data sets obtained from a Ni(111) crystal in a picture frame geometry as shown in Fig. 6 and from polycrystalline silver.

Fig. 9 shows normal emission spectra from silver as measured with the three channeltron detectors and one of the Mott polarimeters. As a measure for the detection efficiency, the step height of the Fermi edge is indicated. A pass energy of $E_P = 5$ eV in the analyzer and $E'_P = 1.5$ keV in the transport lens was chosen. The Mott detectors were operated at 50 kV. From the ratio of channeltron counts to Mott detector

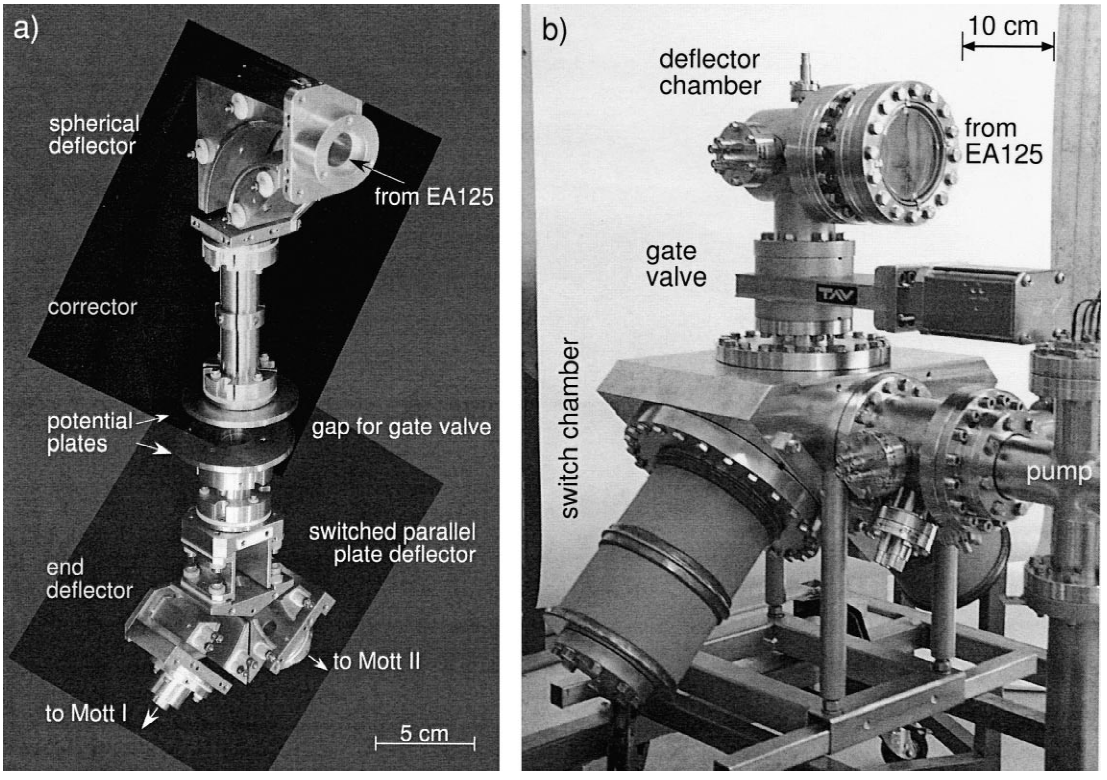

Fig. 8. (a) Photograph of the aluminum lens electrodes for the beam transport system. A total of 14 different voltages are applied to individual elements. (b) Photograph of the vacuum envelope of the beam transport and polarimeter system including the ceramics insulators of the two Mott detectors (test set-up).

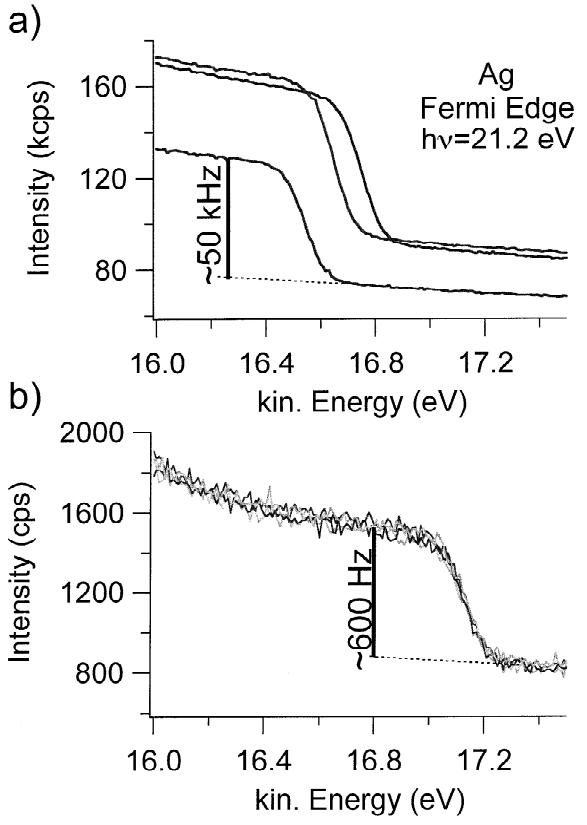

Fig. 9. Fermi edge spectra of freshly sputtered polycrystalline silver as seen by the three channeltrons (a) and four Mott detector channels (b). All data were measured simultaneously in one scan. The scales are uncorrected: the different energy positions due to different exit slit locations can be seen as well as the different detection efficiencies.

counts the transmission through the beam transport lens is estimated to be very high. An instrumental energy resolution of around 100 meV for the channeltrons and 120 meV for the Mott detectors was determined from the spectra in Fig. 9. These values can be further improved by choosing lower pass energies.

The Ni(111) sample was prepared by the standard procedure of Ar^+ sputtering and annealing to ca. 1000 K. It was magnetized by high-current pulses (50 A during 2 ms) through the heating and magnetizing Ta filament. The remnant magnetization proved to be rather low. It appears to be limited by the shape of the picture frame crystal [40] and the compromise between magnetizing current and sample heating.

To determine the direction of magnetization, secondary electrons excited with UV light from the He lamp were measured in normal emission. Fig. 10a shows the measured asymmetries A_x (polarimeter II) and A_y (polarimeter I) as a function of the azimuthal angle φ of the sample, which determines the matching of the magnetization direction with the sensitive axes of the polarimeters in this normal-emission geometry. To eliminate instrumental asymmetries, the measurements were performed after magnetizing the sample with current pulses of both polarities, and the cross-asymmetries were calculated as

$$A^{\otimes} = \frac{(N_{\mathrm{L}}^{\oplus} + N_{\mathrm{R}}^{\ominus}) - (N_{\mathrm{R}}^{\oplus} + N_{\mathrm{L}}^{\ominus})}{(N_{\mathrm{L}}^{\oplus} + N_{\mathrm{R}}^{\ominus}) + (N_{\mathrm{R}}^{\oplus} + N_{\mathrm{L}}^{\ominus})} \tag{12}$$

where $N^{\oplus}$ and $N^{\ominus}$ denote measurements with the respective magnetization polarities and L, R have to be replaced by the appropriate channels as shown in Eq. (10). The statistical error of $A^{\otimes}$ can be calculated analogous to Eq. (9). From these data the in-plane component of the magnetization vector in the sample coordinates was reconstructed according to Eq. (11) as

$$\begin{aligned} A_x^{(\mathrm{S})} &= 1/\sqrt{2}\left[(\cos\varphi - \sin\varphi)A_x^{\otimes} - (\cos\varphi + \sin\varphi)A_y^{\otimes}\right] \\ A_y^{(\mathrm{S})} &= 1/\sqrt{2}\left[(\sin\varphi + \cos\varphi)A_x^{\otimes} - (\sin\varphi - \cos\varphi)A_y^{\otimes}\right] \end{aligned} \tag{13}$$

Fig. 10b shows the resulting asymmetry vectors in the sample surface plane. They fall mostly into the same quadrant and cluster around the indicated vector, which lies between the $[\bar{2}11]$ and the $[1\bar{0}1]$ directions. The easy magnetization axes of nickel are the $\langle 111\rangle$ (easiest) and $\langle 110\rangle$ (second easiest) type axes. The absolute value of the asymmetry is 0.3%. Assuming a Sherman function of $S = 15$–25%, this corresponds to a polarization of $P = 1.2$–2%. For a fully magnetized sample a secondary electron polarization of 8% (at 2 eV kinetic energy) is expected [41], therefore a degree of magnetization of 15–25% of the saturation magnetization can be estimated. The out-of-plane component $A_z^{(\mathrm{S})}$ was found to be zero within the error bars indicating an average magnetization direction in the surface plane. This result demonstrates the capability of COPHEE to perform three-dimensional spin-polarimetry.

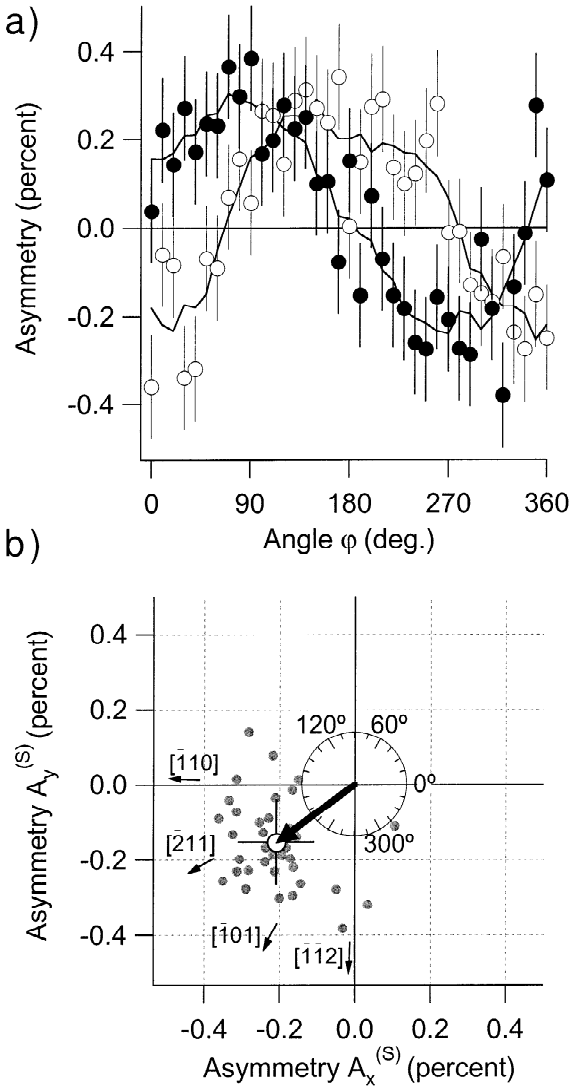

Fig. 10. (a) Asymmetries $A_x^{\otimes}$ (white circles) and $A_y^{\otimes}$ (black circles) for normal emission secondary electrons at $E_{kin} = 2$ eV excited with UV light from a He lamp in Ni(111), calculated according to Eq. (12). The azimuthal angle φ of the sample was varied to rotate the sample magnetization direction in the *xy*-plane. The two sensitive axes of the Mott polarimeters show a sine modulation of the data. Smoothed data are shown as a guide to the eye. (b) Reconstructed asymmetry vectors ($A_x^{(S)}$, $A_y^{(S)}$) according to Eq. (13) in the sample coordinate system. Individual reconstructions at each angular setting from (a) are represented as grey dots, the mean vector is shown as a black arrow. Only components parallel to the surface plane are shown. The magnitude of the asymmetry and the corresponding polarization values are discussed in the text.

To investigate the spin polarization of individual bands we chose a region in the nickel Fermi surface where a clear assignment to (minority) d-bands and spin-split pairs of sp-bands could be given in previous studies [21]. The $\bar{1}\bar{1}$2 scans were carried out at $\vartheta = 78°$ around the [$\bar{1}\bar{1}$2] azimuth as indicated by the arrow in Fig. 3b. The procedure of reversing the magnetization by a current pulse in between subsequent scans was applied again. Fig. 11 shows the measured intensities (spin integrated data) and asymmetries $A_z^{\otimes}$. In this near-grazing emission geometry, the largely in-plane magnetization vector has a strong component along the *z*-axis of the Mott detector system when the sample azimuth is chosen appropriately. No background subtraction was performed. The asymmetries were measured by the two individual Mott polarimeters quasi-simultaneously by switching the electron beam at 1 Hz between polarimeter I and polarimeter II. The measured

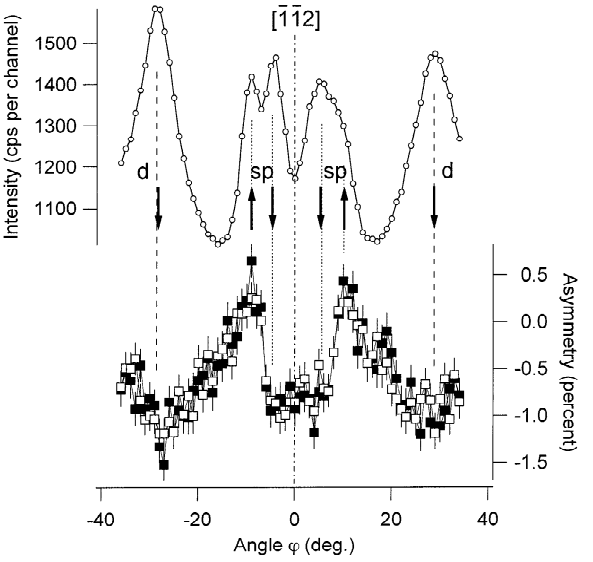

Fig. 11. He Iα excited Fermi edge angular distribution curve from Ni(111) along the path indicated in Fig. 3. The upper part shows the spin integrated intensity with the known spin assignment to individual bands. In the lower part the measured asymmetries $A_z^{\otimes}$ are shown. The white squares (polarimeter I) and black squares (polarimeter II) were measured by the two independent Mott detectors quasi-simultaneously. The maximum asymmetry contrast $\Delta A_z = A_z^{\uparrow} - A_z^{\downarrow} = 1.2\%$ between majority and minority sp-bands corresponds to a polarization-contrast $\Delta P_z \simeq 6\%$ again indicating a poorly magnetized sample.

asymmetries were found to be larger than those of the secondary electrons (Fig. 10) indicating a strong polarization of these electrons photoemitted by direct transitions from the Fermi level. The overall measuring time for this data set, from which a spin-resolved momentum distribution curve can be obtained, was 2.5 h.

6. Conclusions and outlook

We have emphasized the necessity to combine high resolution angle-scanned photoelectron spectroscopy and spin detection for the investigation of surface and thin film magnetism. The interplay between magnetic properties and electronic structure requires a surface sensitive Fermi surface probe with spin resolution. The technique of Fermi surface mapping by angle resolved photoemission proves suitable for such systems, and the use of Mott detectors in conjunction with Fermi surface mapping equipment was discussed. The requirement for measuring the full spin polarization vector in these experiments is satisfied using two independent, orthogonally mounted Mott detectors. We have described the conception and the design of this complete photoemission experiment extensively. First experiments on Ni(111) show the capability of the instrument to measure the polarization as a vector quantity and to determine the spin character of electronic states at the Fermi level. The ultimate energy and angular resolution of this spin-resolved electron spectrometer is an unprecedented 15 meV and $\pm 1°$, respectively and is thus sufficient to address many of the problems discussed in the introduction.

The spin resolution can now be used for three purposes. First, the sign of the polarization gives information on the spin character of electronic states. Second, the degree of spin polarization can be measured and therefore the degree of magnetisation for individual states can be measured, e.g. in temperature-dependent studies. Third, the position and width of peaks in the polarization signal can be used for a more precise determination of binding energies and momenta and it can even resolve spectral features that might not be visible in spin integrated spectroscopies.

In the future the instrument can be used for a variety of investigations. (i) For bulk magnetic materials the technique of Fermi surface tomography using various photon energies at a synchrotron light source allows the mapping of the complete Fermi surface of a material as seen through its surface. Magnetically active regions can therefore be identified. (ii) Thin films of magnetic materials as well as combinations of magnetic and non-magnetic layers, and the coupling between different layers, can be investigated. Specifically the spin character of the electronic states can now be revealed. (iii) The interplay between surface magnetism and adsorbates can be studied both by monitoring the reaction of substrate bands to adsorbed molecules and by measuring induced magnetism in the adsorbate itself. (iv) In addition to the ARUPS regime the instrument can also be used for spin-polarized core level studies in X-ray photoelectron, Auger electron and resonant photoemission spectroscopies.

Acknowledgements

We wish to thank Drs Iwao Matsuda, Luc Patthey, Christoph Quitmann and Ralph E. Pixley for many fruitful discussions. Dr Giorgio Rossi first proposed the use of two independent Mott detectors. Drs Detlef Vermeulen, Steve Hunt and Markus Janousch of the SLS Computing and Controls group provided hardware and conceptual support for the EPICS-based data acquisition system. We are greatly indebted to the staff of the mechanical workshop of the Physics Institute in Zurich, in particular to B. Schmid, P. Treier and B. Wachter and to the group technician W. Deichmann. Financial support from the Swiss National Science Foundation (REQUIP 21-53281.98 in collaboration with D. Pescia, ETH Zurich and P. Aebi, University of Fribourg) is gratefully acknowledged.

References

[1] F.J. Himpsel, J.E. Ortega, G.J. Mankey, R.F. Willis, Adv. Phys. 47 (1998) 511.
[2] G.A. Prinz, Science 282 (1998) 1660;
S.A. Wolf, D.D. Awschalom, R.A. Buhrman, J.M. Daughton,

S. von Molnár, M.L. Roukes, A.Y. Chtchelkanova, D.M. Treger, Science 294 (2001) 1488.
[3] J.E. Ortega, F.J. Himpsel, Phys. Rev. Lett. 69 (1992) 844.
[4] B.G. Briner et al., Europhys. News 28 (1997) 149.
[5] R.H. Gaylord, K. Jeong, S.D. Kevan, Phys. Rev. Lett. 62 (1989) 203.
[6] A. Santoni, L.J. Terminello, F.J. Himpsel, T. Takahashi, Appl. Phys. A52 (1991) 229.
[7] P. Aebi, J. Osterwalder, R. Fasel, D. Naumovic, L. Schlapbach, Surf. Sci. 307–309 (1994) 917.
[8] J. Osterwalder, Surf. Rev. Lett. 4 (1997) 391.
[9] P. Aebi, T.J. Kreutz, J. Osterwalder, R. Fasel, P. Schwaller, L. Schlapbach, Phys. Rev. Lett. 76 (1996) 1150.
[10] T. Greber, T.J. Kreutz, J. Osterwalder, Phys. Rev. Lett. 79 (1997) 4465.
[11] H.C. Siegmann, F. Meier, M. Erbudak, M. Landolt, Adv. Electron. Electron Phys. 62 (1984) 1, and references therein.
[12] K.-P. Kämpfer, W. Schmitt, G. Güntherodt, Phys. Rev. B 42 (1990) 10696.
[13] W.H. Butler, X.-G. Zhang, D.M.C. Nicholson, T.C. Schulthess, J.M. MacLaren, Phys. Rev. Lett. 76 (1996) 3216.
[14] C.T. Chen, J. Electron Spectrosc. Relat. Phenom. 92 (1998) 289.
[15] F. Manghi, V. Bellini, J. Osterwalder, T.J. Kreutz, P. Aebi, C. Arcangeli, Phys. Rev. B 59 (1999) R10409.
[16] J. Osterwalder, J. Electron Spectrosc. Relat. Phenom. 117–118 (2001) 71.
[17] P.J. Feibelman, D.E. Eastman, Phys. Rev. B (1974) 104932.
[18] C.N. Berglund, W.E. Spicer, Phys. Rev. A 136 (1964) 1030 and 1044.
[19] S. Hüfner, Photoelectron Spectroscopy, Springer, Berlin, 1995.
[20] E. Bertel, M. Donath (Eds.), Electronic Surface States and Interface States on Metallic Systems, World Scientific, Singapore, 1995.
[21] T.J. Kreutz, T. Greber, P. Aebi, J. Osterwalder, Phys. Rev. B 58 (1998) 1300.
[22] N.F. Mott, Proc. R. Soc. Lond., Ser. A 124 (1929) 425; N.F. Mott, Proc. R. Soc. Lond., Ser. A 135 (1932) 429.
[23] N. Sherman, Phys. Rev. 103 (1956) 1601.
[24] J. Kessler, Polarized Electrons, 2nd Edition, Springer, Berlin, 1985.
[25] V.N. Petrov, M. Landolt, M.S. Galaktionov, B.V. Yushenkov, Rev. Sci. Instrum. 68 (1997) 4385.
[26] V.N. Petrov, M.S. Galaktionov, A.S. Kamochkin, Rev. Sci. Instrum. 72 (2001) 3729.
[27] M. Landolt, D. Mauri, Phys. Rev. Lett. 49 (1982) 1783.
[28] S. Qiao, A. Kimura, A. Harasawa, M. Sawada, J.-G. Chung, A. Kakizaki, Rev. Sci. Instrum. 68 (1997) 4390.
[29] L.G. Gray, M.W. Hart, F.B. Dunning, G.K. Walters, Rev. Sci. Instrum. 55 (1984) 88.
[30] S. Qiao, A. Kakizaki, Rev. Sci. Instrum. 68 (1997) 4017.
[31] G.C. Burnett, T.J. Monroe, F.B. Dunning, Rev. Sci. Instrum. 65 (1994) 1893.
[32] J. Kirschner, Polarized Electrons at Surfaces, Springer, Berlin, 1985.
[33] J. Unguris, D.T. Pierce, R.J. Celotta, Rev. Sci. Instrum. 57 (1986) 1314.
[34] see http://www.psi.ch/sls/
[35] see http://www.elettra.trieste.it/
[36] P. Baltzer, L. Karlsson, M. Lundquist, B. Wanneberg, Rev. Sci. Instrum. 64 (1993) 2179.
[37] T. Greber, O. Raetzo, T.J. Kreutz, P. Schwaller, W. Deichmann, E. Wetli, J. Osterwalder, Rev. Sci. Instrum. 68 (1997) 4549.
[38] The crystal was grown and cut by MaTecK Material-Technologie & Kristalle GmbH, 52428 Jülich, Germany.
[39] 'SIMION 3D Version 6.0' by David A. Dahl, 43rd ASMS Conference on Mass Spectrometry and Allied Topics, May 21–26 1995, Atlanta, GA, p. 717; http://www.srv.net/~klack/simion.html
[40] M. Donath, Surf. Sci. Rep. 20 (1994) 251.
[41] M. Landolt, Spin Polarized Secondary Electron Emission from Ferromagnets, in: R. Feder (Ed.), Polarized Electrons in Surface Science, World Scientific, Singapore, 1985.